

High-resolution forest carbon stocks and emissions in the Amazon

Gregory P. Asner^{a,1}, George V. N. Powell^b, Joseph Mascaro^a, David E. Knapp^a, John K. Clark^a, James Jacobson^a, Ty Kennedy-Bowdoin^a, Aravindh Balaji^a, Guayana Paez-Acosta^a, Eloy Victoria^c, Laura Secada^d, Michael Valqui^d, and R. Flint Hughes^e

^aDepartment of Global Ecology, Carnegie Institution for Science, Stanford, CA 94305; ^bWorld Wildlife Fund, Washington, DC 20090; ^cPeruvian Ministry of Environment, Lima 27, Peru; ^dWorld Wildlife Fund, Lima 14, Peru; and ^eInstitute of Pacific Islands Forestry, United States Forest Service, Hilo, HI 96720

Edited by B. L. Turner, Arizona State University, Tempe, AZ, and approved August 10, 2010 (received for review April 9, 2010)

Efforts to mitigate climate change through the Reduced Emissions from Deforestation and Degradation (REDD) depend on mapping and monitoring of tropical forest carbon stocks and emissions over large geographic areas. With a new integrated use of satellite imaging, airborne light detection and ranging, and field plots, we mapped aboveground carbon stocks and emissions at 0.1-ha resolution over 4.3 million ha of the Peruvian Amazon, an area twice that of all forests in Costa Rica, to reveal the determinants of forest carbon density and to demonstrate the feasibility of mapping carbon emissions for REDD. We discovered previously unknown variation in carbon storage at multiple scales based on geologic substrate and forest type. From 1999 to 2009, emissions from land use totaled 1.1% of the standing carbon throughout the region. Forest degradation, such as from selective logging, increased regional carbon emissions by 47% over deforestation alone, and secondary regrowth provided an 18% offset against total gross emissions. Very high-resolution monitoring reduces uncertainty in carbon emissions for REDD programs while uncovering fundamental environmental controls on forest carbon storage and their interactions with land-use change.

deforestation | forest degradation | Peru | Reduced Emissions from Deforestation and Degradation | United Nations Framework Convention on Climate Change

Between 10% and 15% of global carbon dioxide emissions originate from deforestation and degradation of tropical forests (1, 2). Emblematic of these emissions, the southwestern Peruvian Amazon is undergoing carbon changes via road building, mining, timber extraction, and farming. Meanwhile, the United Nations Framework Convention on Climate Change is working to develop a program to curb carbon emissions via the program for Reduced Emissions from Deforestation and Degradation (REDD) (3, 4). REDD has the potential to connect carbon emitters with governments positioned to reduce forest carbon losses through monetary compensation. In addition to offsetting emissions, REDD could provide indirect support for biodiversity conservation through reduced habitat loss, thus providing a unique solution to the longstanding tension between conservation interests and other land-use needs in tropical forest regions such as the Peruvian Amazon.

There are many challenges to making REDD work, and mapping forest carbon stocks and emissions at the high resolution demanded by investors and monitoring agencies remains a technical barrier. Satellite remote sensing offers a practical means to monitor forest cover (5, 6), but has not provided high-resolution estimates of carbon emissions (7). In contrast, field plots provide effective localized estimates of forest carbon stocks, but natural variation in forest carbon density may render plot-based approaches ineffective for estimating carbon over large areas. Furthermore, although plot-based studies are needed for long-term monitoring of forest dynamics, they are time-consuming and are usually placed to avoid land-use change, which is the main anthropogenic factor responsible for carbon flux to the atmo-

sphere in tropical forests. New approaches are critically needed to extend the role of field plots to capture regional variation and to bridge a major gap between field and satellite observations.

One new approach is airborne light detection and ranging (LiDAR), which, when used with field calibration plots, is capable of estimating aboveground forest carbon densities (in units of Mg C ha^{-1}) (8). However, airborne LiDAR has not been proven for carbon mapping of high diversity Amazon forests, and a key obstacle to large-scale use of LiDAR for REDD monitoring is its relatively high cost of operation and small geographic coverage. However, combined with a strategic use of satellite data, airborne LiDAR may yield cost-effective, high-resolution maps of forest carbon stocks and emissions (9). This potential has never been realized at large geographic scales that would be pertinent to an international REDD program.

Here we report on a study to apply a new multiscale, multi-temporal method to analyze carbon stocks and emissions throughout 4.3 million ha of lowland Amazon forest in the Department of Madre de Dios, Peru, as a procedure for achieving national-scale REDD mapping while assessing determinants of biomass stocks at a large geographic scale. Although subnational within Peru, the study area is equivalent to twice that of Costa Rica's forests, and our study was designed with a survey size that is logistically easy to implement multiple times to achieve necessary coverage for larger nations. The Madre de Dios region has undergone relatively moderate land-use change throughout the past century. However, paving of the Interoceanic Highway since 2006, along with new timber concessions and an influx of artisanal gold miners during the past 5 y, has rapidly increased land-use pressure. In this context, we sought to understand the sources of spatial and temporal variability in carbon stocks and emissions throughout this large and rapidly changing region of the Amazon basin. Our approach involves multiscale steps ranging from automated satellite mapping of deforestation and degradation to airborne LiDAR mapping to local-scale plot calibration measurements. The approach provides high-resolution maps of aboveground carbon densities and a retrospective mapping of carbon emissions based on current carbon densities and past forest cover changes (*SI Materials and Methods*).

Results and Discussion

Airborne LiDAR data yielded forest canopy height, underlying terrain, and canopy vertical profile, providing a comprehensive,

Author contributions: G.P.A. and G.V.P. designed research; G.P.A., G.V.P., J.M., D.E.K., J.K.C., J.J., T.K.-B., G.P.-A., E.V., L.S., M.V., and R.F.H. performed research; G.P.A., J.M., D.E.K., J.K.C., J.J., T.K.-B., and A.B. analyzed data; and G.P.A. and J.M. wrote the paper.

The authors declare no conflict of interest.

This article is a PNAS Direct Submission.

Freely available online through the PNAS open access option.

¹To whom correspondence should be addressed. E-mail: gpa@stanford.edu.

This article contains supporting information online at www.pnas.org/lookup/suppl/doi:10.1073/pnas.1004875107/-DCSupplemental.

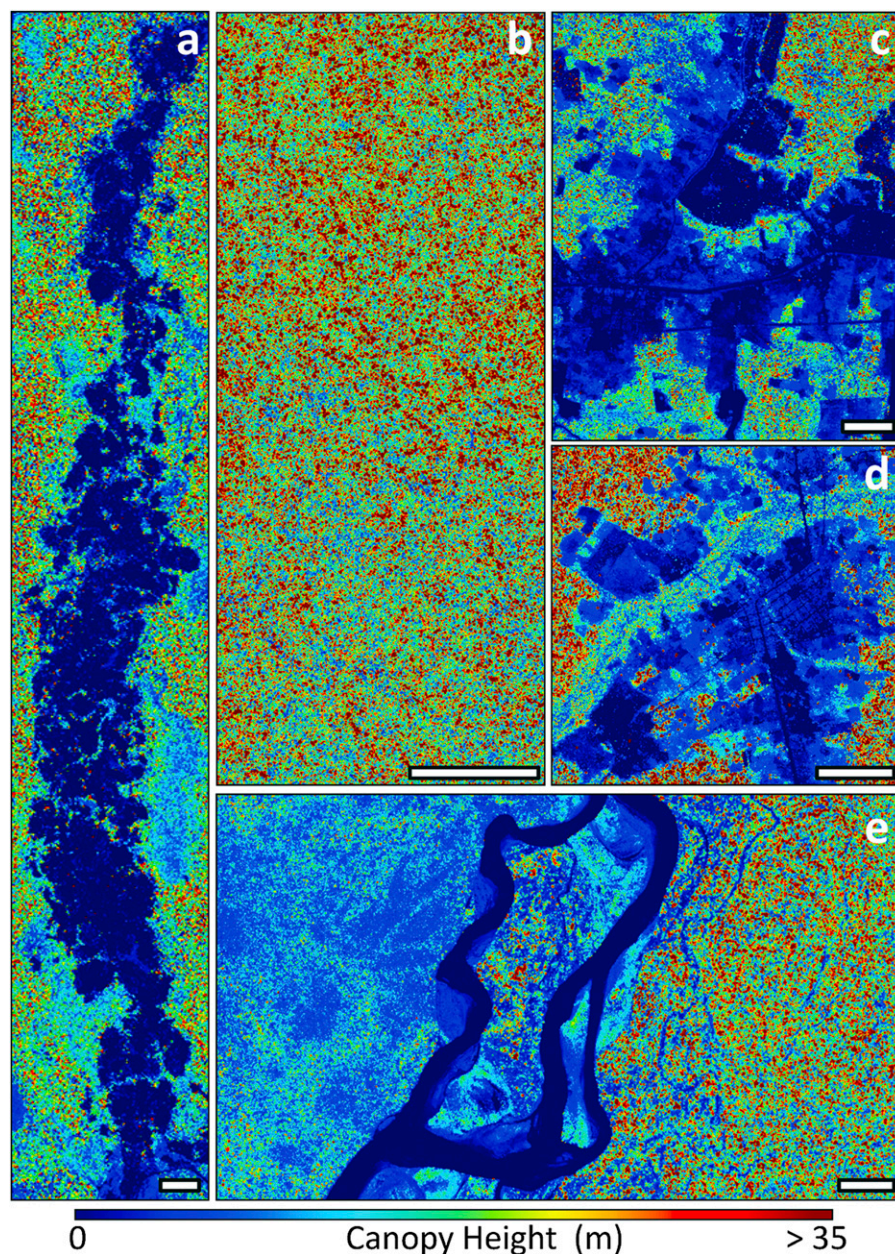


Fig. 1. Sources of variation in forest canopy height detected with high-resolution Carnegie Airborne Observatory LiDAR in the Peruvian Amazon: (A) artisanal gold mining; (B) selective logging; (C) deforestation for cattle ranching; (D) infrastructural development in towns, cities, and supporting land uses; and (E) alluvial and geologic substrate. White bars indicate a distance of 0.5 km in each example image.

regional inventory of both human-mediated and natural variation in Amazon forest canopy structure. Snapshot areas of 8,000 to 50,000 ha in size are shown in Fig. 1, each indicative of a major source of variation in canopy structure and carbon stocks throughout the region. Gold mining spans large areas of lowland swamp forest, leaving bare surface scars of up to 20 km in length with almost no remaining tree cover (Fig. 1A). Degradation from selective logging results in a spatially diffuse decrease in canopy height in otherwise intact forest (blue areas of Fig. 1B). Farming, cattle ranching (Fig. 1C), and infrastructural development (Fig. 1D) are major drivers of deforestation, leaving mosaics of depleted carbon stocks with diffusely scattered tree cover along roadways and in clearings. Finally, by virtue of being regional-scale, the data allowed us to assess gradients in forest structure mediated by geomorphic and fluvial processes (Fig. 1E).

During LiDAR overflights, a small, tactically placed network of field plots was established to convert LiDAR metrics of forest canopy structure to aboveground carbon density (Fig. S1). Extensive field validation, including both new and previously published estimates from field plots in the region (10, 11), indicated a LiDAR-to-carbon measurement correlation of 92% (Figs. S4–S6). Absolute mapping uncertainties were 23 Mg C ha^{-1} at 0.1 ha resolution, but decreased to just 5 Mg C ha^{-1} , or approximately 5% of the mean standing forest biomass stock, when the mapping results were integrated to 5 ha resolution (Figs. S7 and S8).

Application of LiDAR-based carbon statistics to forest type and condition maps derived from satellite data (SI Materials and Methods) yielded a 0.1-ha resolution map of aboveground carbon density throughout the 4.3 million ha region (Fig. 2). Total regional carbon storage was 395 Tg (million metric tons), and three

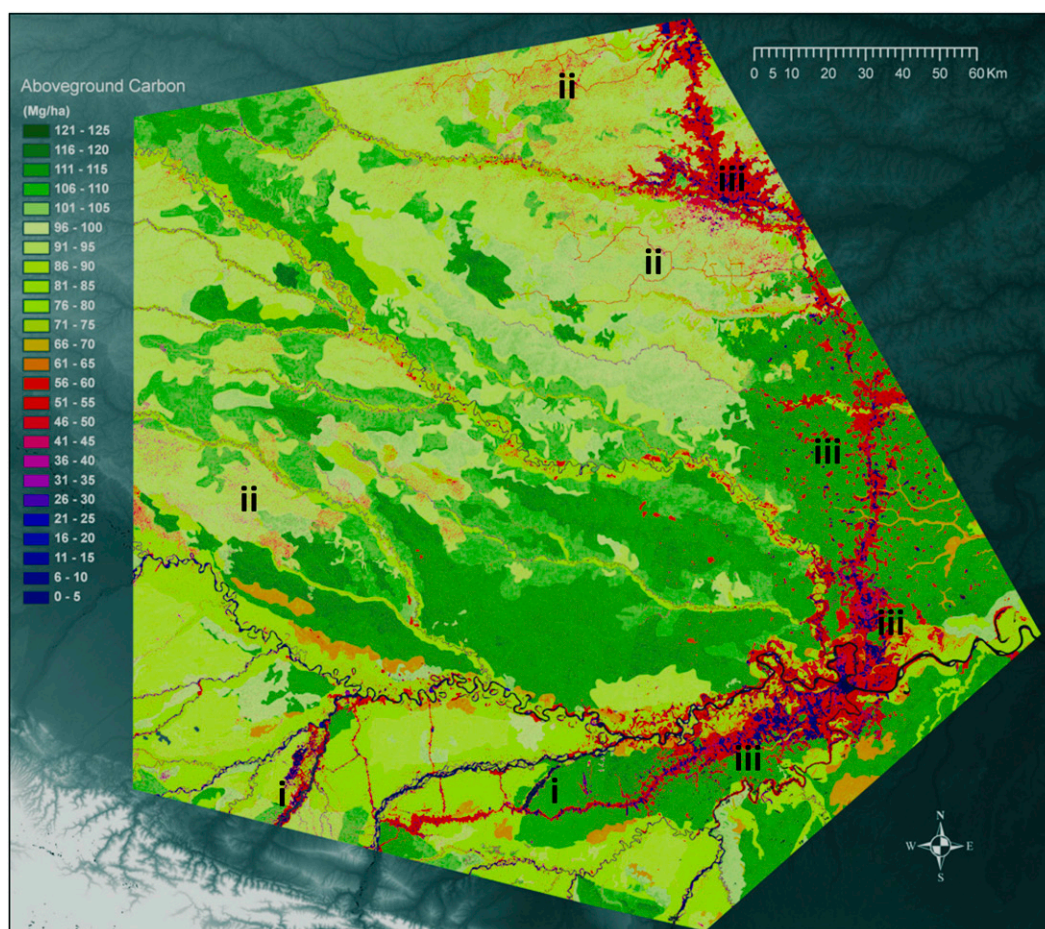


Fig. 2. Variation in aboveground carbon storage at 0.1 ha resolution throughout a 4.3 million ha region of the Peruvian Amazon, derived from an integrated use of CLASlite, LiDAR and field-plot data. Examples of (i) artisanal gold mining, (ii) selective logging and other forest disturbances, and (iii) deforestation for cattle ranching, road building, and other infrastructure are indicated.

major sources of variation in forest carbon were uncovered. First, we found a broad regional partitioning of standing carbon stocks mediated by geologic substrate (12, 13). To the north, older tertiary substrates support carbon densities with median values ranging from 85 to 100 Mg C ha^{-1} , whereas more fertile and flat Holocene alluvial surfaces in the central-east support 110 to 125 Mg C ha^{-1} . To the southwest, forests at the base of the Andes on Cretaceous surfaces maintain carbon densities in the range of 65 to 80 Mg C ha^{-1} (t test comparisons on randomly selected subsets, $P < 0.001$).

Stepping down in geographic scale from geologic controls, we uncovered enormous variation in standing carbon within and among forest types (Fig. 3A and Fig. S9). Median carbon density values were unique between forest types in most cases ($P < 0.001$; Fig. 2), but the highly varying distributions were the most revealing of ecological controls (Fig. 3A). Upland *terra firme* forests on low hills maintain the highest and widest range of carbon stocks, whereas inundated swamp areas with often monotypic palm cover are confined to a lower and narrower range of carbon storage conditions. Still wetter swamp forests with a dense shrub layer harbor even lower and narrower distributions of carbon. Areas that undergo periodic disturbance, such as floodplain forests and river edges, have highly skewed, multimodal distributions of carbon density, indicating a patch mosaic of distinct successional states. Finally, areas codominated by hardwood species and bamboo also show a bimodal distribution of carbon states.

Against this backdrop of geological and ecological control on carbon storage, the most pronounced, localized sources of carbon variation are deforestation, degradation, and secondary regrowth (Fig. 2). Although only 5% in geographic extent (Table 1), artisanal mine sites contain the lowest carbon densities among all land-use scenarios, just 16.7 ± 18.3 (SD) Mg C ha^{-1} . Selective logging and other forms of forest degradation are common, especially to the north, and account for 27% of the pixel-by-pixel changes in forest cover during the study period (Table 1). Forest degradation is diffusely distributed over large areas, but the individual pixels impacted within these areas support carbon stocks of only 35.6 ± 15.4 Mg C ha^{-1} , which is approximately 70% lower than background forest levels. Deforestation accounted for nearly 68% of forest loss throughout the region from 1999 to 2009. However, we found that deforestation results in a wide range of residual carbon stocks on the land: areas averaging 20% tree cover maintain 15.9 ± 32.8 Mg C ha^{-1} , whereas those maintaining at least 60% cover support 61.4 ± 56.2 Mg C ha^{-1} (Fig. S10).

Integrating historical deforestation and degradation results (Figs. S2 and S3) with 2009 carbon stocks (Fig. 2), we calculated annual gross aboveground carbon emissions from 1999 to 2009 (Fig. 3B). Results show a baseline emission rate for 1999 to 2006 of 0.26 ± 0.08 Tg C yr^{-1} from deforestation and 0.11 ± 0.02 Tg C yr^{-1} from degradation, for a sum of 0.37 Tg C yr^{-1} . Paving of the Intercoastal Highway since 2006, combined with new timber logging concessions and gold mining, caused an increase in deforestation emissions by more than 61% to 0.42 ± 0.21 Tg C yr^{-1} ,

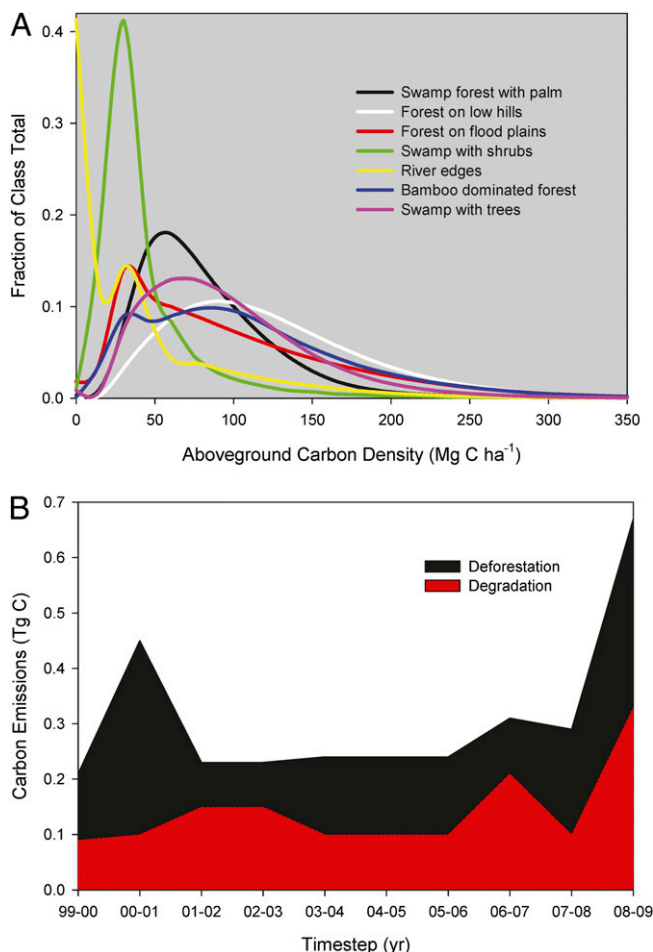


Fig. 3. (A) Distributions of aboveground carbon storage for the seven common forest types found in the Peruvian Amazon, derived from airborne LiDAR. (B) Annual emissions of carbon from deforestation and degradation mapped from time-series CLASlite imagery and LiDAR data.

whereas degradation emissions doubled to $0.21 \pm 0.11 \text{ Tg C yr}^{-1}$ (Fig. 3B). Critically, we found that degradation emissions averaged 47% of deforestation emissions (annual range, 22%–68%) during the 11-y study period, both before and during the recent increase in human activity throughout the region. In total, 4,529 Tg of aboveground carbon were committed to the atmosphere from 1999 to 2009, representing approximately 1.1% of the standing stock of forest carbon in the region.

Secondary forest regrowth, defined here as forests reestablished following any deforestation and degradation that occurred between 1999 and 2008, covered 24,823 ha in the study region.

representing 38% of the total human-affected area by 2009 (Table 1). Forest regrowth resulted in a range of carbon densities (24–44 Mg C ha⁻¹) based on forest ages of 2 to 11 y (*SI Materials and Methods*). Nonetheless, the carbon density of secondary forest is 30.6 ± 16.7 Mg C ha⁻¹, or approximately 60% to 70% lower than the average carbon stocks for intact forests in the region. Integrated over the 11-y study period, secondary regrowth accumulated 0.812 Tg C, providing an 18% offset to gross emissions that resulted in a net regional loss of 3.717 Tg C to the atmosphere.

Our results uncover multiple spatial scales of variation in carbon stocks throughout the region, and change our understanding of how forest carbon is distributed and subsequently altered by land-use change in the southwestern Amazon. To our knowledge, this is the first study to detail regional-level variation in forest carbon densities mediated by geologic substrate and forest type (Figs. 2 and 3.4). We also detected an interaction between geological controls on carbon storage and land-use effects on carbon emissions: deforestation emissions dominated the flatter quaternary substrates that are easier to access for road-building and farming. In contrast, degradation emissions from selective logging occurred mostly on eroded tertiary surfaces that are topographically dissected and difficult to access (Fig. 2).

The observed trend of increasing carbon emissions since 2006 following the development of the Interoceanic Highway is previously unmeasured (Fig. 3B), but more revealing is the large contribution of degradation to the total annual gross emissions for the region. Degradation added an average of 47% more carbon to the atmosphere than did deforestation alone, and increased in step with deforestation during the recent period of heightened land-use activity in the region. Degradation is diffusely distributed throughout the forested landscapes of Amazonia and other tropical regions, and only by combining very high-resolution airborne LiDAR techniques with large-area satellite mapping can these emissions be quantified and monitored over time.

The detailed statistical distributions of aboveground carbon density were also previously unmeasured because the majority of the region remains inaccessible on the ground. However, our airborne measurements reveal highly skewed, often multimodal, distributions of forest carbon. As a result, we contend that samples of forest carbon storage obtained with field plots, cannot account for the spatial variation in carbon stocks, especially in the context of the mosaic of anthropogenic land uses and resulting carbon emissions.

In support of REDD, the Intergovernmental Panel on Climate Change (IPCC) (14) issued a default tier-I estimation approach of forest carbon density based on average carbon values assigned for biomes. Applying the IPCC tier-I method to our study region produced an estimated 587 Tg C in aboveground biomass, whereas our spatially explicit mapping indicated just 395 Tg C (Fig. 2). This difference results primarily from the fact that forest carbon densities are not homogeneous at a variety of scales. Although our regional carbon estimates are 33% lower than IPCC tier-I estimates, the high-resolution, verifiable nature of our ap-

Table 1. Area of new land use and forest regrowth integrated from 1999 to 2009

Land use	Total area, ha	Proportion of human-affected area, %	Mean (SD) carbon density, Mg C ha ⁻¹
Gold mining	3,207	4.9	16.7 (18.3)
Forest degradation*	17,740	27.3	35.6 (15.4)
Deforestation†	43,933	67.7	27.8 (16.9)
Secondary regrowth‡	24,823	38.3	32.7 (7.5)

Mean aboveground carbon densities are reported for 2009.

*Forest degradation is dominated by selective logging in this region.

[†]Deforestation is dominated by clearing for cattle ranching and farming in this region.

[‡] Regrowth calculated from deforestation and disturbance mapped between 1999 and 2008.

proach would likely yield increased investment per unit of carbon (15, 16). At the national scale, most tropical countries will rely initially on tier-I methods, which will generate large uncertainties and lower confidence, and thus potentially lower carbon credits (4, 15, 17). Developing monitoring capacities at higher accuracies—using procedures like those demonstrated here—will ultimately provide increased carbon credit, boosted carbon sequestration, and improved biodiversity protection.

The cost to implement this method of high-resolution carbon stock and emissions monitoring is decreasing. Satellite data costs are decreasing, and the major data sources are now free of charge to end users. The cost for analyzing the satellite data for forest cover, deforestation and degradation is also rapidly diminishing. The Carnegie Institution is making its Landsat Analysis System Lite (CLASlite) available for free to noncommercial organizations throughout the Amazon region (<http://claslite.ciw.edu>). LiDAR is a powerful airborne imaging technology that, like aerial photography in the 1970s and 1980s, is rapidly expanding throughout the world for use across a range of environmental sectors. There are now many airborne LiDAR mapping companies operating in the Americas, Europe, Africa, Asia, Australia, and the Pacific (<http://www.airbornelasermapping.com>). For this 4.3 million ha analysis, the Carnegie Airborne Observatory (CAO) operated its LiDAR, processed the data, and provided maps of forest structure at a cost of less than \$0.08/ha. More recent work in Madagascar has reduced the cost to approximately \$0.06/ha, and there exists a strong economy-of-scale effect whereby larger-area projects prove far more cost effective than small-area analyses. This runs opposite to plot-level work, which increases in cost on a per-area basis.

Finally, the procedure tested here can be scaled up to the national level. We selected this particular 4.3 million ha area for a variety of scientific purposes. The results can be directly extrapolated with the addition of highly available satellite imagery and CLASlite, and with no additional airborne or ground-based work, to an area of approximately 60 million ha based on the range of forest types found in Peru. However, the uncertainty in the regional variation of carbon densities applied to such a full

national-scale satellite map would be reduced with additional LiDAR sampling throughout the region. Here we have reported the results of high-resolution mapping of carbon stocks and emissions in the Amazon region, and the approach is being implemented by three western Amazon countries.

Materials and Methods

Our approach involves four steps: (i) regional mapping of vegetation type and condition (forest cover, deforestation, degradation, regrowth) using moderate-resolution satellite data; (ii) regionally stratified large-area sampling of vegetation canopy 3D structure using airborne LiDAR; (iii) conversion of LiDAR vegetation structural data to aboveground carbon density using LiDAR allometrics developed at a limited number of field plots; and (iv) integration of the satellite maps with the calibrated LiDAR data to set a regional, high-resolution baseline carbon estimate, and mapping of carbon emissions retrospectively and into the future.

Forest condition—including deforestation, degradation, and regrowth—was assessed using the CLASlite (18) satellite mapping system with 30-m Landsat imagery in nearly annual time steps from 1999 to 2009 (Figs. S1–S3). Field validation surveys indicated that 2009 deforestation, degradation, and secondary regrowth maps had errors of 0% to 1.2%, 1.9% to 6.4%, and 2.6% to 2.9%, respectively (Tables S1 and S2). A map partitioning the study area into 26 vegetation classes, combined with CLASlite results, was used to locate 27 LiDAR survey areas covering a total of 514,317 ha for collection at a spatial resolution of 1 m or less throughout the 4.3 million ha region (Fig. S1). The LiDAR data were collected using the CAO (19). Calibration and validation of the airborne- and satellite-based estimates of aboveground carbon density were carried out during the overflights. Detailed information on each of these steps is provided in *SI Materials and Methods*.

ACKNOWLEDGMENTS. We thank G. Agosti, M. E. Arroyo, L. Carranza, J. A. Escudero, A. Felix, A. Forsyth, N. Jarmillo, K. Ledesma, A. Mulanovich, R. E. Martin, C. Moran, J. C. Rivera, A. Rosenthal, and C. Verastegui for logistical and field assistance; T. Baker and the RAINFOR Network for providing field data for LiDAR validation work; and Bosque Sociedad y Desarrollo Institution, H. Duenas, the herbarium of the National University of Madre de Dios, the Protected Areas Natural Service (SERNANP), and especially the Amazon Conservation Association for logistical assistance. This project was supported by the Government of Norway, Gordon and Betty Moore Foundation, Carnegie Institution, W. M. Keck Foundation, and William Hearst III.

- IPCC (2007) *Climate Change 2007: Impacts, Adaptation and Vulnerability* (Cambridge Univ Press, New York).
- van der Werf GR, et al. (2009) CO₂ emissions from forest loss. *Nat Geosci* 2:737–738.
- Olander LP, Gibbs HK, Steininger M, Swenson JJ, Murray BC (2008) Reference scenarios for deforestation and forest degradation in support of REDD: A review of data and methods. *Environ Res Lett* 3:025011.
- Angelsen A (2008) Moving Ahead with REDD: Issues, Options and Implications (Center for International Forestry Research, Bogor, Indonesia).
- Hansen MC, et al. (2008) Humid tropical forest clearing from 2000 to 2005 quantified by using multitemporal and multiresolution remotely sensed data. *Proc Natl Acad Sci USA* 105:9439–9444.
- Achard F, et al. (2007) Pan-tropical monitoring of deforestation. *Environ Res Lett* 2: 1–11.
- Global Observation of Forest and Land Cover Dynamics (2008) *Reducing Greenhouse Gas Emissions From Deforestation and Degradation in Developing Countries: A Sourcebook of Methods and Procedures for Monitoring, Measuring and Reporting*. (Natural Resources Canada, Calgary, AB, Canada).
- Lefsky MA, et al. (2002) Lidar remote sensing of above-ground biomass in three biomes. *Glob Ecol Biogeogr* 11:393–399.
- Asner GP (2009) Tropical forest carbon assessment: Integrating satellite and airborne mapping approaches. *Environ Res Lett* 3:03009.
- Phillips OL, et al. (1998) Changes in the carbon balance of tropical forests: Evidence from long-term plots. *Science* 282:439–442.
- Anderson LO, et al. (2009) Influence of landscape heterogeneity on spatial patterns of wood productivity, wood specific density and above ground biomass in Amazonia. *Biogeosciences* 6:1883–1902.
- Campbell KE, Jr, Heizler M, Frailey CD, Romero-Pittman L, Prothero DR (2001) Upper Cenozoic chronostratigraphy of the southwestern Amazon Basin. *Geology* 29:595–598.
- Sombroek W (2000) Amazon landforms and soils in relation to biological diversity. *Acta Amazonica* 31:81–100.
- Eggleston HS, Buendia L, Miwa K, Ngara T, Tanabe K, eds (2006) *2006 IPCC Guidelines for National Greenhouse Gas Inventories*. Intergovernmental Panel on Climate Change. (Institute for Global Environmental Strategies, Kanagawa, Japan).
- Mollicone D, et al. (2007) Elements for the expected mechanisms on “Reduced Emissions from Deforestation and Degradation (REDD)” under UNFCCC. *Environ Res Lett* 2:045024.
- Giacomo G, et al. (2008) Applying the conservativeness principle to REDD to deal with the uncertainties of the estimates. *Environ Res Lett* 3:035005.
- Gibbs HK, Brown S, Niles JO, Foley JA (2007) Monitoring and estimating tropical forest carbon stocks: Making REDD a reality. *Environ Res Lett* 2:1–13.
- Asner GP, Knapp DE, Balaji A, Paez-Acosta G (2009) Automated mapping of tropical deforestation and forest degradation: CLASlite. *J Appl Remote Sens* 3:033543.
- Asner GP, et al. (2007) Carnegie Airborne Observatory: In-flight fusion of hyperspectral imaging and waveform light detection and ranging (LiDAR) for three-dimensional studies of ecosystems. *J Appl Remote Sens* 1:1–21.

Supporting Information

Asner et al. 10.1073/pnas.1004875107

SI Materials and Methods

Overview of Approach. Our approach supports IPCC (1) tier-II/III baseline assessments via high-resolution aboveground carbon stock and emissions mapping (Fig. S1). Five major steps are involved: (i and ii) regional mapping of vegetation type and condition (forest cover, deforestation, degradation, regrowth) using moderate-resolution satellite data; (iii) regionally stratified large-area sampling of vegetation canopy 3D structure using airborne LiDAR; (iv) conversion of LiDAR vegetation structural data to aboveground carbon density using LiDAR allometrics developed at a limited number of field plots; and (v) integration of the satellite maps with the calibrated LiDAR data to set a regional, high-resolution baseline carbon estimate, and mapping of carbon emissions over time.

The first step involves the acquisition and/or development of a map depicting major vegetation types (Fig. S1A). In recent years, many such maps have become available at national and subnational levels. Some of these maps are derived from satellite data; others are created from a combination of aerial photography and field surveys. A map of forest types aids in partitioning a region into categories for subsequent airborne and field measurements. The more detailed the map, the more finely the landscape can be partitioned for biomass sampling. We used the official forest map provided by the Peruvian Ministry of Environment (Ministerio del Ambiente; MINAM), which had 26 vegetation classes. The map coverage extent was 4,369,972 ha, defining the overall study region.

We used CLASlite (<http://claslite.ciw.edu>) to extend the generic MINAM vegetation map to include current forest conditions (Fig. S1B). Maps of deforestation and degradation were compiled with an historical analysis of Landsat 5 Thematic Mapper and Landsat 7 Enhanced Thematic Mapper Plus (ETM+) imagery for the years 1999 to 2001, 2003, and 2006 to 2009. We first created a map of regional forest cover in 2009. Forest/nonforest in this year was mapped automatically using the CLASlite software in single-image analysis mode (2). CLASlite uses a combination of atmospheric correction, spectral mixture analysis, and decision tree analysis to map forest cover at 30 m spatial resolution when using Landsat Thematic Mapper or ETM+ imagery. Using CLASlite in multiimage analysis mode (2), we then mapped gross deforestation and degradation in each of seven time steps (1999–2000, 2000–2001, 2001–2003, 2003–2006, 2006–2007, 2007–2008, and 2008–2009). CLASlite detects and maps deforestation according to the algorithms detailed by Asner et al. (2). Here we define degradation as a diffuse thinning of or disturbance to forest cover, and CLASlite has algorithms for detecting this disturbance uniquely from wholesale deforestation (2). For this study, we also passed a 3×3 (90 m) median filter over the CLASlite degradation output, which removed single, isolated pixels that would represent natural treefall events. To ensure that final maps reflected accurate stages of regrowth in 2009, forest change maps were prioritized through the 10-y period, by year, to count only the most recent event of forest change. These CLASlite steps yielded final maps of forest cover and nonforest cover with deforestation, degradation, and forest regrowth by year for the period 1999 to 2009 (Figs. S2 and S3). CLASlite maps of deforestation, degradation, and regrowth were field-tested as described in a subsequent section.

After spatially integrating the MINAM and CLASlite maps, the region was stratified into LiDAR mapping units (Fig. S1C). The extent of airborne LiDAR required to accurately characterize carbon stocks among vegetation types throughout a given mapping region will depend on the relative proportions of each veg-

etation type and the likely variation of carbon densities within each type. Based on minimum sampling trials undertaken for other forests, we strived to achieve at least 1% LiDAR coverage of each vegetation class with and without forest degradation. However, based on other scientific interests, we exceeded the minimum coverage by mapping 1.5% to 33.9% of most vegetation classes (Table S1). Three exceptions resulted in less than 0.5% coverage per vegetation class, but these classes represented less than 1% of the study area. Two classes—forest on low hills with rubber tree stands and forest on medium terraces with swamped area—were aggregated into two larger vegetation classes: forest on high hills with rubber tree stands and forest on medium terraces, respectively, based on input from MINAM biologists.

The CAO (<http://cao.ciw.edu>) collected the LiDAR data used in this study. The flights were conducted in two modes: (i) high-resolution (1,000 m above ground level, 0.5-m LiDAR spot spacing, 22° field of view, 70-kHz pulse repetition frequency) and (ii) low-resolution (2,000 m above ground level, 1.0-m LiDAR spot spacing, 28° field of view, 50 kHz pulse repetition frequency). For both flight modes, the aircraft maintained a ground speed less than 95 kn. LiDAR spatial error is less than 0.15 m vertically and less than 0.36 m horizontally [rms error (rmse)] (3). Flights were planned to sample forest (and other) vegetation using parallel flight lines with 50% overlap to ensure full and consistent coverage. The total LiDAR coverage was 514,317 ha or approximately 12% of the study area.

Following airborne LiDAR sampling, the mapped canopy 3D structural information was used to estimate aboveground carbon density (in Mg C ha^{-1} ; Fig. S1D). This step requires a set of LiDAR metrics. Ground-based allometric equations have been used for decades to estimate aboveground biomass from field measurements of tree diameters, tree height, and wood density (4, 5). In contrast, LiDAR metrics are new; they relate airborne measurements of forest 3D structure, including height and the vertical canopy profile, to field-based estimates of aboveground biomass. Whereas the basic LiDAR data are typically collected at a spatial resolution of 0.5 to 1.0 m, LiDAR metrics are averaged at the plot level and subsequently regressed against plot-level aboveground carbon stock estimates. This approach parallels traditional field studies that use manual measurements of the diameter and height of each tree to estimate plot-level C stocks. Details on LiDAR-to-carbon metrics are provided in a subsequent section.

Output from the LiDAR mapping step includes estimates of aboveground carbon density at 0.1-ha resolution, along with error values derived from uncertainty in the LiDAR-to-C conversion equations used. The final step involved developing statistical distributions of aboveground carbon densities for each MINAM vegetation class, in areas with and without forest degradation, as well as deforested areas and areas of secondary forest regrowth (Fig. S1E). The median carbon value of each distribution by class was then applied to the integrated MINAM–CLASlite maps through time (1999–2009). A final step included scaling the carbon values by the amount of canopy opening (or loss) derived from the fractional canopy cover mapping step of CLASlite, detailed by Asner et al. (6, 7) and described in a subsequent section.

Validation of Forest Cover, Deforestation, Degradation, and Regrowth. Forest cover, deforestation, degradation, and regrowth maps representing 2009 conditions were validated using a combination of methods. The high-resolution airborne LiDAR and hyperspectral imagery from the CAO provided more than 500,000 ha of vali-

dation imagery at 0.5 to 1.0 m spatial resolution. These data were used to assess forest cover and degradation caused by logging and other small-scale human activities in forests. A survey was done by overlaying the CAO imagery onto the CLASlite (Landsat) imagery and manually delineating differences in forest cover and degradation between the two data sources. As the CAO data provide tree-level spatial resolution, we treated these data as “truth.” Any discrepancies, in terms of false-negatives or false-positives, between the CAO and CLASlite imagery were then digitally marked and tabulated. This step yielded an estimated error rate of 11.5 Landsat pixels per 10,000 pixels (0.115% error) for forest cover, and these were about equally distributed among false-positive and false-negative forest detections. Some exceptions included areas of active deforestation, where the offset in time between Landsat and CAO overpasses allowed for forest clearing to occur. The error rate for degradation averaged 154 Landsat pixels per 10,000 pixels, or 1.54%, in areas of selective logging. Error rates appeared slightly higher (2%–3%) in areas near towns where human activities are more pronounced; we could not assess the cause of these errors but assumed they were again caused by offsets in the time of Landsat and CAO imaging.

A second validation technique involved field-based surveys of deforestation and degradation from the 2008–2009 time period, as well as regrowth from the period from 2000 to 2009. These field-based surveys used roads, trails, and rivers to digitally mark false positives and false negatives using a tablet computer system with integrated global positioning system (iX104C4; Xplore Technologies). The surveys were undertaken outside of the LiDAR coverage, but within the CLASlite image coverage. For practical purposes, degradation was considered as any loss of forest canopy in a single pixel otherwise immediately surrounded by remaining forest cover. In addition, a new handheld data collection/cellular telephone technology with integrated cameras and global positioning system was used to collect detailed information about forest cover, composition of forested and cleared areas, and other ancillary data. These units use the Open Data Kit software tools (<http://code.google.com/p/open-data-kit/>) to collect, organize, and map field data directly into the CLASlite imagery. The results of these surveys are provided in Table S2. Errors for 2009 forest cover and 2008–2009 deforestation ranged from 0% to 1.8%. Uncertainties in 2008–2009 degradation and 2000–2009 regrowth were 1.9% to 6.4% and 2.6% to 2.9%, respectively. Thus, all error levels were small and well within the tolerable limits for mapping carbon stocks and emissions at the regional level.

LiDAR Calibration Using Field Plots. There are multiple ways to relate LiDAR measurements to aboveground carbon density. Lefsky et al. (8) derived LiDAR metrics for three temperate and boreal forest biomes. As a result of high structural complexity and canopy stratification, tropical and subtropical ecosystems have posed a greater challenge. Although equations were developed by Drake et al. (9) for moist and wet tropical forests, they used a large-footprint LiDAR technology unique to NASA’s research program. Asner et al. (10) derived equations relating airborne, small-footprint LiDAR metrics to carbon densities for lowland, submontane, and montane tropical forests. However, regional variation in wood density, stem diameter, and the number of trees per unit area creates regional variation in the LiDAR-to-carbon relationship. As a result, field plots are needed to calibrate the relationship between LiDAR metrics and aboveground carbon stocks for different forests (11). Field plots can be set up anywhere within the LiDAR coverage area, but should span a range of apparent carbon levels and forest types. The number of field plots required to create a reliable LiDAR-to-carbon relationship is a focus of intense research, and thus we provide detailed analysis of our findings here. If the time-consuming process of placing field plots can be reduced in scope to the role of LiDAR calibration, then the LiDAR becomes the regional sampling tool,

mapping thousands of hectares per day in a way that is unachievable with field plots.

Field plots. To calibrate LiDAR metrics of aboveground carbon, we established 131 large field plots (radius 30 m, area per plot 0.2827 ha, total area 37 ha), and 37 small field plots (radius 3 m, area per plot 28.27 m², total area 1,046 m²) distributed among 10 common vegetation classes in the study area. Within each large plot, we measured the diameter of all living and standing dead stems larger than 10 cm. Trees and palms were included if at least 50% of the base occupied the plot, whereas lianas were included if they crossed a plane at 1.3 m in height above the plot footprint as they ascended into the canopy. Accounting for lianas crossing the plane of 1.3 m in height allows for more rapid assessment without differences in density or basal area measurements (12). All trees were measured at 1.3 m height or above buttress. When an above-buttress measurement could not be obtained by hand, a digital photograph was taken and the tree diameter estimated by comparing the pixel width of the tree to a 1-m reference placed in the photograph (13). Within a one-eighth section of each large plot (northwest to north), we also measured the diameter of all living and standing dead stems at least 5 cm. Within each small plot, we harvested all living and standing dead aboveground vegetation smaller than 10 cm in diameter and weighed it in the field using spring scales.

Estimation of aboveground carbon stocks. We estimated aboveground carbon stocks in the large plots using allometric models. We first accounted for dead trees and nontree growth forms, such as palms, bamboo, and lianas, by using growth form-specific allometric models (Table S3). We measured the height of all palms and dead trees using laser range finders. For all other individuals, we used a generalized allometric model from Chave et al. (5), which, in addition to diameter, requires inputs of wood density and height. We identified 98.2% of living stems to genus, and obtained a genera-specific wood density estimate from a global wood density database for 91.4% of living stems (data available upon request). Although identification to species can improve wood density estimation, Baker et al. (14) found that genera-level identification accounted for 71% of wood density variation in the tropics. We accounted for height variation using a combination of direct measurements (with either laser range finders or clinometers) and diameter-based estimation. We measured the height of the three largest-diameter trees in each plot (e.g., those with the greatest importance to carbon estimation) as well as seven or more additional trees in each plot spanning a range of diameters. These tree height data were used in two ways: (i) measured trees retained their measured heights for input into the Chave et al. (5) allometric model, and (ii) 1,681 total height measurements were used for the creation of a diameter-to-height model that was used to estimate the height of all other trees (Fig. S44). The selection of a single diameter-to-height model was made after variation in diameter-to-height relationships by habitat type was found to be nonsignificant. Within each small plot, we harvested all living and standing dead aboveground vegetation and weighed it in the field using spring scales. We collected a representative subsample (approximately 5% by mass) of the harvested vegetation that was weighed immediately in the field and oven-dried to constant mass to correct for moisture content. We multiplied all biomass estimates by 0.48 to estimate carbon content.

Development of LiDAR-to-carbon models. We developed LiDAR-based models to estimate aboveground carbon separately for vegetation at least 10 cm in diameter and that smaller 10 cm in diameter. In each case, we considered models based on three previously tested LiDAR-based metrics of the vertical profile of the forest: (i) mean canopy profile height (MCH), (ii) top-of-canopy height, and (iii) quadratic mean canopy profile height. For vegetation at least 10 cm in diameter, all three metrics produced highly significant LiDAR-to-carbon relationships, but the MCH was the best overall predictor of aboveground carbon (Fig. S4B).

To estimate carbon in vegetation less than 10 cm in diameter, we combined two sets of field plot data: (i) harvest-based estimates of aboveground carbon from the 3-m radius plots, and (ii) allometry-based estimates of aboveground carbon from the one-eighth subsample in the 30-m radius plots (excluding large plots with a mean MCH below approximately 13 m, which was the highest MCH sampled by the small plots). In examining these datasets, we found that the presence of bamboo stems was not a factor in aboveground carbon storage for the small plots, but was a strong factor in aboveground carbon storage in the large plots. Thus, we created two separate sets of LiDAR-to-carbon models for vegetation smaller than 10 cm in diameter: one for bamboo habitat types and one for those without bamboo. As with larger vegetation, we found that MCH was the best overall predictor of aboveground carbon in this small size class (Fig. S4C). Our carbon estimates for vegetation smaller than 10 cm in diameter excluded stems smaller than 5 cm in diameter for dense forest (e.g., MCH greater than approximately 13). However, outside estimates suggest that the contribution to carbon storage for stems smaller than 5 cm in diameter in such forests is very low (15). When the results of the equations were combined to produce a synthetic relationship between MCH and aboveground carbon density, we found that the variation in carbon as predicted by MCH was strongly consistent across all 10 habitat types sampled (Fig. S5A). Thus, LiDAR-derived MCH accounted for wide variation in forest age, structure, and diversity.

Other allometric models. When one generalized allometric model is used to estimate the carbon stocks of nearly all trees (as in this study), the choice of the model to be used has a major influence on the resulting estimates. To consider this effect, we examined the range of carbon estimates and LiDAR-to-carbon models that might be produced if other equations were to be used. We compared our Chave et al. (5)-based estimates to three other models (Figs. S5B and S6A). A model proposed by Baker et al. (16) yielded an underestimate compared with the Chave (5) model, whereas other models proposed by Winrock International and Chave (model II) (17, 18) produced large overestimates of carbon stocks. Whereas the primary model used here [Chave model I (5)] incorporates an independent height variable in the allometric equation, the models by Baker and Winrock (16, 18) instead use regional measurements of height to adjust the allometric equation constants. Chave model II (17) uses no height variable or height variation adjustment. Thus, we used the most robust model available in that it corrects for height variation of individual trees. The wide variation among methods with varying treatments of canopy height suggests that correcting for height is essential to producing accurate carbon stock estimates (19). Specifically, forests in the Southwestern Amazon (such as those studied here) are typically shorter than those in the Central Amazon, resulting in somewhat lower carbon stocks in aboveground biomass.

Validation of Remotely Sensed Carbon Stocks. We verified our LiDAR-to-carbon model for stems at least 10 cm in diameter using two datasets: (i) 28 additional 0.28-ha plots, and (ii) nine 1-ha plots from the RAINFOR plot network (20), none of which were used in the calibration phase of the study. The added 0.28-ha plots used an identical methodology. The 1-ha plots are part of the RAINFOR forest dynamics network and use similar methodology with two exceptions. First, their allometric model differed slightly from that used here. However, as with our approach, tree height and wood density variation were accounted for based on local patterns. Second, dead trees were not included in the RAINFOR carbon estimates.

The LiDAR data were a strong predictor of standing carbon (≥ 10 cm dbh) in the validation plots, explaining 92% of the variation (Fig. S6B). A regression model fit to the validation plots alone had a slope that was nearly identical to that of the

original calibration model (Fig. S6C). We note that the strength of fit was higher than for the original calibration data ($r^2 = 0.86$). In part, the stronger fit of the calibration model to the validation data may be explained by the inclusion of the 1-ha plots. These larger plots represent an area larger than three of our 0.28-ha plots combined. Over this spatial scale, estimation errors in standing carbon are predicted to average out, resulting in improved regressions (see subsequent section on error analysis).

Error Analyses for LiDAR-to-Carbon Relationships. Spatial propagation of error in LiDAR data. The primary LiDAR-to-carbon model used in this study has a SE of estimate (SEE) of ± 23.56 Mg C ha $^{-1}$. However, this error estimate applies to the spatial scale of one of our field plots (0.28 ha), such that the total uncertainty of carbon predicted for a new field plot would be ± 6.66 Mg carbon. For an area of interest of larger size (such as any reasonably sized land holding), the uncertainty depends on the spatial propagation of the error. Because SEs scale according to the square root of the sum of squares, total error increases at a slower rate than total carbon. As a result, the SE (on a per-area basis) for carbon density estimates decays with increasing sample area.

When adding plot carbon totals and SEs, the total error (ϵ) for a given number of plots (n) is given by:

$$\epsilon_{\text{Mg}} = \sqrt{\sum_{i=1}^n \text{SEE}_{i(\text{Mg})}^2} \quad [\text{S1}]$$

If we assume that carbon densities within an area are centered on the mean carbon density for that area, Eq. 1 can be approximated as:

$$\epsilon_{\text{Mg}} = \text{SEE}_{(\text{Mg})} * \sqrt{n} \quad [\text{S2}]$$

If we then let x = sample area (ha) (where $x = n * 0.2827$ ha), we produce the following estimation of total error:

$$\epsilon_{\text{Mg}} = 6.6604 * \sqrt{\left(\frac{x}{0.2827}\right)} \quad [\text{S3}]$$

Finally, we can readjust to SE on a per-area sampled basis by dividing by x :

$$\text{SEE}_{\frac{\text{Mg}}{\text{ha}}} = \frac{6.6604 * \sqrt{\left(\frac{x}{0.2827}\right)}}{x} \quad [\text{S4}]$$

The relationship between sample area and per-area SE is one of precipitous decline in error with increasing sample area (Fig. S7). Consider a 0.28-ha region of interest (e.g., one of our study plots) which has a predicted total carbon density of 28.27 Mg (e.g., 100 Mg C ha $^{-1}$). From our LiDAR-to-carbon relationship, we predict a SE of ± 6.66 Mg carbon at this spatial scale. However, if we double the area of interest (to 0.56 ha), total carbon increases to ± 56.54 Mg, but the total error according to Eq. 2 is now given by $\sqrt{(2 * \text{SE}^2)}$, or $6.66 * 1.41$, which is ± 9.42 Mg carbon. Although the total error increases, the relative error decreases from 24% to 17%. When corrected for area, the SE effectively decreases from ± 23.56 to ± 16.66 Mg/ha, or by 29%. Results in Fig. S7A also highlight the fact that, at 5 ha mapping resolution, the absolute uncertainty in LiDAR-derived carbon densities diminishes to approximately 5 Mg carbon ha $^{-1}$, which is just 4% to 5% of the median carbon density of most forest types throughout the region.

To further demonstrate the spatial propagation of error, we simulated a doubling of sample area by aggregating our plots and observing the change in SEE between LiDAR-derived MCH and aboveground carbon. We ranked all plots according to MCH, and merged odd-ranked plots with even-ranked plots (1 and 2, etc.) to create 0.56-ha aggregate plots. We found that whereas the

slope of the MCH-to-carbon relationship was unchanged, the SEE declined from ± 23.56 to ± 18.25 Mg carbon ha⁻¹. This 23% decline in SEE was close to the 29% we found using the simulation, and reflects the same precipitous decline in SEE with increasing sample area.

Neither of these exercises considers the error produced by our equations used to estimate low biomass. However, this error is very low (± 2 – 3 Mg C ha⁻¹) even at the very small spatial scale of our small plots (28.27 m²). Due to the pattern described earlier, any error at these low biomass levels would be obscured even at the minimum spatial scale considered by the large plots (0.2827 ha).

Number of field plots required for LiDAR calibration. To assess the sensitivity of the LiDAR-to-carbon regression to the number of field plots measured, we tested the variability of the regression results by randomly leaving multiples of 5% of the samples out of the regression and calculating the SEE for each resulting regression equation. We repeated this 1,000 times, with each run removing and adding back a random set of six field plots. This allowed us to characterize the error inherent in the model as we produce regression equations with a larger number of samples. Fig. S8 (red line) indicates that the SEE initially increases as the number of samples increases in the regression model. It then begins to asymptote at 15 to 20 plots, whereafter adding more plots only changes the SEE by approximately 1 Mg carbon ha⁻¹. The additional plots do not significantly add to characterizing the relationship between the LiDAR metric and aboveground carbon stocks.

The predictive power of the regression was then assessed by calculating the rmse of a set of independent ($n = 7$) samples, which were not used in developing the regression equation. We repeated this analysis 1,000 times with regression models that increased in sample size from 5% to 95% of the original data set. Fig. S8 (blue line) indicates an initial rapid decline in rmse from approximately 28 Mg carbon ha⁻¹ when 5% ($n = 7$ plots) are used in the regression to approximately 23 Mg carbon ha⁻¹ when 20% ($n = 24$ plots) are used. Thereafter, as the number of plots is increased, the predictive error only decreases to 22 Mg carbon ha⁻¹. This finding concurs with ref. 11, which indicated that fewer and fewer plots will be needed for LiDAR calibration in the future as the slope of the LiDAR-to-carbon regression equation will simply require adjustment to local conditions based on a tactical (i.e., cost-effective) use of field plots.

Calculation of Regional Carbon Stocks. Combining the MINAM vegetation map, the 2009 CLASlite forest condition maps, and LiDAR-based images of aboveground carbon density (Mg ha⁻¹), we calculated statistics for each forest type as well as for nonforest cover and regrowth areas. Nonforest cover, defined by a CLASlite decision tree based on the 2009 fractional canopy cover output (2), was further partitioned into four subsets according to the fraction of photosynthetic vegetation (PV) in each nonforest pixel. In this case, PV fraction is an excellent proxy for partial tree cover remaining in otherwise nonforest (e.g., open cattle pasture) pixels (21). By applying the LiDAR-based carbon densities that covered areas of different fractional PV cover in these clearings, we were able to quantify carbon stocks at different levels of partial deforestation. Regrowth areas were partitioned by year of most recent deforestation or degradation.

In most cases, the distributions of carbon stocks were highly skewed for intact, partially deforested, and regrowing forests (Figs. S9 and S10). This precluded the use of means and variances to describe the data or to apply the statistics to the regional map. Instead, for each forest type, the median carbon density results from LiDAR survey of each vegetation type were applied to the combined MINAM and 2009 CLASlite map at 0.1 ha resolution.

The resulting median map was further processed by integrating 2009 CLASlite fractional canopy cover output, as described in detail by Asner et al. (6, 7), to up- and down-regulate the median

carbon density values on a pixel by pixel basis. Regression analysis showed that the fraction of bare soil (from CLASlite spectral mixture analysis) is inversely correlated with carbon density values from the LiDAR survey. Therefore, we applied the equation:

$$C_{\text{pixel}} = C_{\text{median}} * (1.0 - \text{Bare}_{\text{pixel}}) \quad [\text{S5}]$$

Eq. 5 serves to decrease carbon density from the class median when woody or herbaceous canopy cover decreases within a pixel. Practically, this often occurs in the most heavily deforested areas as well as in areas of maximum forest degradation. Through additional analyses of the relationships between CLASlite fractional cover and LiDAR-based carbon densities, we also found that a decrease in the amount of standing dead or senescent vegetation, known as nonphotosynthetic vegetation (22), from the modal nonphotosynthetic vegetation value for a given vegetation class is inversely proportional to carbon density. This inverse relationship is caused by variations in the areal density of tree crowns that allow for the exposure of surface litter to the satellite sensor (23), and thus we applied the equation:

$$C_{\text{pixel}} = C_{\text{median}} * [1.0 + (\text{NPV}_{\text{mode}} - \text{NPV}_{\text{pixel}})] \quad [\text{S6}]$$

Functionally, Eq. 5 had the largest effects in deforested areas, with departures from the class median carbon density values by 2 to 25 Mg ha⁻¹. Use of Eq. 6 had a smaller effect of 1 to 10 Mg carbon ha⁻¹, and mostly in forested areas.

Calculation of Carbon Emissions. Carbon emissions from deforestation and forest degradation were mapped and compiled using a combination of 2009 LiDAR-derived aboveground carbon stocks in standing forest combined with the time-series analysis of Landsat 5 and Landsat 7 imagery for the years 1999 to 2001, 2003, and 2006 to 2009. The forest change maps were stratified by the MINAM vegetation map to determine the annual area affected by deforestation or degradation. To avoid double counting, forest change maps were prioritized through the 10-y period, by year, to count only the first detection of deforestation or degradation. For example, a pixel classified as deforestation or degradation during the 1999–2000 time step would not be counted as forest change in any subsequent year. Any pixel counted as forest change was assumed to have been intact forest and, as such, was assigned the median carbon value for its corresponding forest type. For both deforestation and degradation, we assume that all carbon in the affected pixel is committed to the atmosphere, which we believe is reasonable at 30-m spatial resolution, as this approaches the size of just one to three tree crowns (24). The forest change areas (in ha) were combined with the median carbon values (Mg ha⁻¹) to calculate gross carbon flux for each time step.

We tabulated annual gross carbon emissions from deforestation dominated by cattle pastures and farms and degradation caused mostly by selective logging, gold mining, and secondary regrowth (Table 1). Areas delineated as deforestation (43,933 ha) and degradation (17,740 ha) from previous steps were used with the exception of two large artisanal gold mining areas totaling 3,207 ha. Secondary forest regrowth totaled 24,823 ha, integrated spatially from previous forest losses in the 1999 to 2008 study period.

IPCC Tier-I Carbon Assessment. The IPCC (1) tier-I approach was applied to the study area using their prescribed forest carbon density values combined with suggested land cover data (25). Land cover type was taken from the Global Ecological Zones according to the methodology developed for the FAO's Forest Resources Assessment 2000 (26). The Global Ecological Zones were then stratified in a geographic information system by a land cover mask generated from the globally available land cover dataset, Global Land Cover 2000 (25, 27). To create the land cover mask, land

cover data were reclassified as forest or nonforest, using all forest classes of GLC 2000. Aboveground carbon densities were assigned to each land cover class using IPCC (1) values. The resulting map

suggests that the total aboveground carbon stock for the region is 587.2 Tg, with a range caused by uncertainty in IPCC tier-I carbon densities of 548.5 Tg, or 93.4% of the mean.

1. Eggleston HS, Buendia L, Miwa K, Ngara T, Tanabe K, eds (2006) *2006 IPCC Guidelines for National Greenhouse Gas Inventories*. Intergovernmental Panel on Climate Change. (Institute for Global Environmental Strategies, Kanagawa, Japan).
2. Asner GP, Knapp DE, Balaji A, Paez-Acosta G (2009) Automated mapping of tropical deforestation and forest degradation: CLASlite. *J Appl Remote Sens* 3:033543.
3. Asner GP, et al. (2007) Carnegie Airborne Observatory: In-flight fusion of hyperspectral imaging and waveform light detection and ranging (LiDAR) for three-dimensional studies of ecosystems. *J Appl Remote Sens* 1:1–21.
4. Brown S, Lugo AE (1984) Biomass of tropical forests: A new estimate based on forest volumes. *Science* 223:1290–1293.
5. Chave J, et al. (2005) Tree allometry and improved estimation of carbon stocks and balance in tropical forests. *Oecologia* 145:87–99.
6. Asner GP, et al. (2005) Selective logging in the Brazilian Amazon. *Science* 310:480–482.
7. Asner GP, et al. (2006) Condition and fate of logged forests in the Brazilian Amazon. *Proc Natl Acad Sci USA* 103:12947–12950.
8. Lefsky MA, et al. (2002) Lidar remote sensing of above-ground biomass in three biomes. *Glob Ecol Biogeogr* 11:393–399.
9. Drake JB, et al. (2003) Above-ground biomass estimation in closed canopy neotropical forests using LiDAR remote sensing: Factors affecting the generality of relationships. *Glob Ecol Biogeogr* 12:147–159.
10. Asner GP, Hughes RF, Varga TA, Knapp DE, Kennedy-Bowdoin T (2009) Environmental and biotic controls over aboveground biomass throughout a tropical rain forest. *Ecosystems (N Y)* 12:261–278.
11. Asner GP (2009) Tropical forest carbon assessment: Integrating satellite and airborne mapping approaches. *Environ Res Lett* 3:03009.
12. Schnitzer SA, DeWalt SJ, Chave J (2006) Censusing and measuring lianas: A quantitative comparison of the common methods. *Biotropica* 38:581–591.
13. Phillips OL, et al. (2009) Drought sensitivity of the Amazon rainforest. *Science* 323:1344–1347.
14. Baker TR, et al. (2004) Variation in wood density determines spatial patterns in Amazonia forest biomass. *Glob Change Biol* 10:545–562.
15. DeWalt SJ, Chave J (2004) Structure and biomass of four lowland neotropical forests. *Biotropica* 36:7–19.
16. Baker TR, et al. (2005) Late twentieth century trends in the biomass of Amazonian forest plots. In *Tropical Forests and Global Atmospheric Change*, eds Malhi Y, Phillips OL (Oxford Univ Press, London), pp 129–141.
17. Chave J, et al. (2005) Tree allometry and improved estimation of carbon stocks and balance in tropical forests. *Oecologia* 145:87–99.
18. Winrock International (2006) *Carbon Storage in the Los Amigos Conservation Concession, Madre de Dios, Perú* (Winrock International, Washington, DC).
19. Nogueira EM, Nelson BW, Fearnside PM, Franca MB, de Oliveira ACA (2008) Tree height in Brazil's 'arc of deforestation': Shorter trees in south and southwest Amazonia imply lower biomass. *Forest Ecol Manage* 255:2963–2972.
20. Baker TR, et al. (2004) Variation in wood density determines spatial patterns in Amazonia forest biomass. *Global Change Biol* 10:545–562.
21. Asner GP, Bustamante MMC, Townsend AR (2003) Scale dependence of biophysical structure in deforested areas bordering the Tapajo's National Forest, Central Amazon. *Remote Sens Environ* 87:507–520.
22. Roberts DA, Green RO, Adams JB (1997) Temporal and spatial patterns in vegetation and atmospheric properties from AVIRIS. *Remote Sens Environ* 62:223–240.
23. Souza C, Roberts DA, Cochrane MA (2005) Combining spectral and spatial information to map canopy damages from selective logging and forest fires. *Remote Sens Environ* 98:329–343.
24. Palace M, Keller M, Asner GP, Hagen S, Braswell B (2008) Amazon forest structure from IKONOS satellite data and the automated characterization of forest canopy properties. *Biotropica* 40:141–150.
25. Gibbs HK, Brown S, Niles JO, Foley JA (2007) Monitoring and estimating tropical forest carbon stocks: Making REDD a reality. *Environ Res Lett* 2:1–13.
26. Food and Agriculture Organization of the United Nations (2001) *Global Forest Resources Assessment 2000*. Available at [ftp://ftp.fao.org/docrep/fao/003/Y1997E/FRA%202000%20Main%20report.pdf](http://ftp.fao.org/docrep/fao/003/Y1997E/FRA%202000%20Main%20report.pdf).
27. Global Land Cover (2000) *Global Land Cover Database* (European Commission, Ispra, Italy).

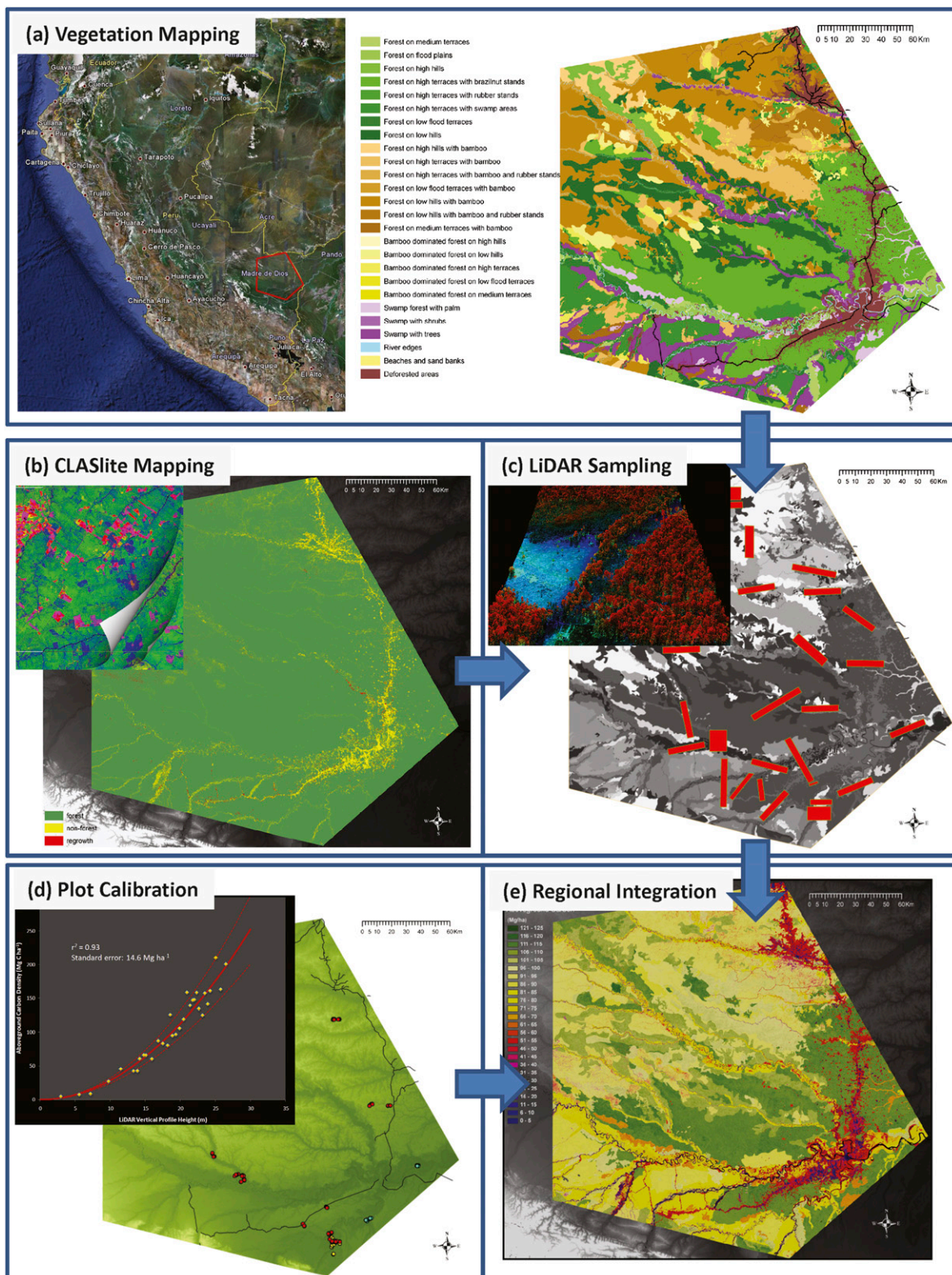


Fig. S1. Illustrated flowchart shows outputs of each major step in our analysis. (A) Location and basic vegetation composition of the 4.3 million ha study area encompassing the cities of Puerto Maldonado and Iberia, Peru, and 25 major forest types. The vegetation map was provided by MINAM. (B) Multitemporal analysis of Landsat imagery using the CLASlite algorithms to map forest cover, deforestation, degradation, and secondary regrowth. (C) Airborne LiDAR sampling (red boxes) of the study region based on the combined MINAM-CLASlite maps to cover at least 1% of each forest type. (D) Calibration of 3D vegetation structural data from LiDAR using a limited number of field plots. (E) Integration of MINAM, CLASlite, and LiDAR data to map aboveground carbon stocks and emissions over the study area at 0.1 ha resolution.

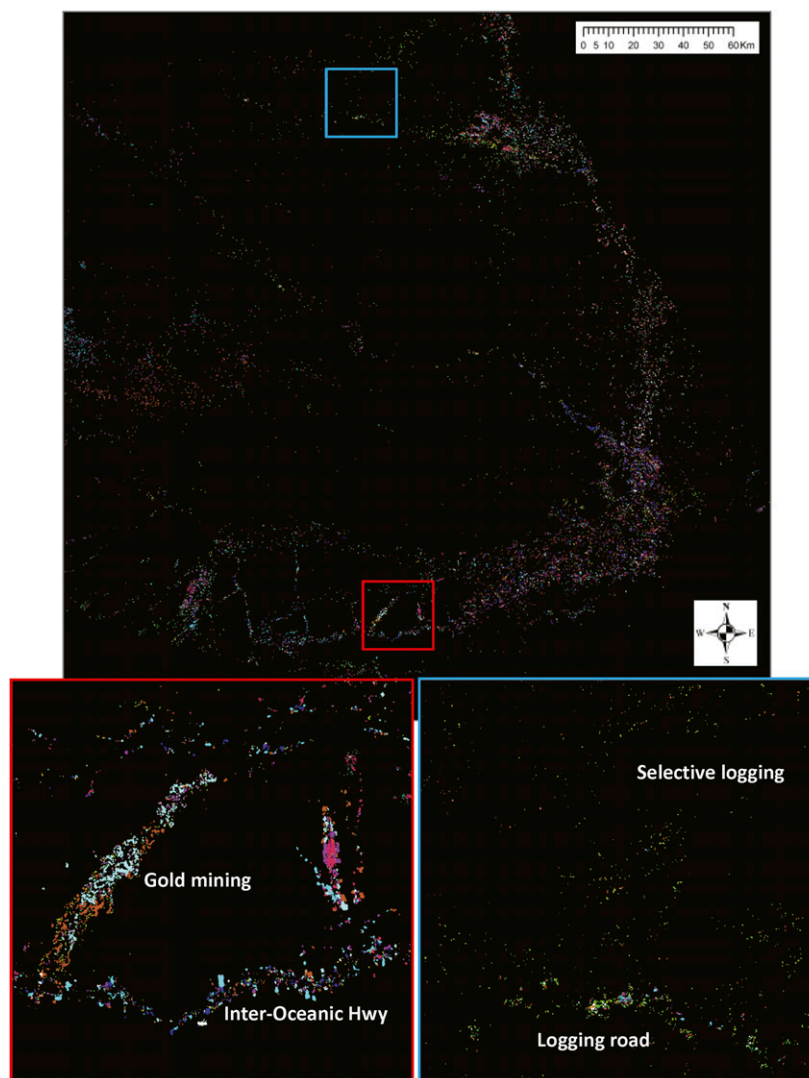


Fig. S2. CLASlite results show deforestation and degradation at 30-m resolution; each color represents a different year between 1999 and 2009. The blue zoom box provides detail showing the spatial patterning of deforestation associated with road building (pasture clearings along the Inter-oceanic Highway) and artisanal gold mining. The red zoom box provides an example of the diffuse thinning of the forest caused by selective logging and associated activities.

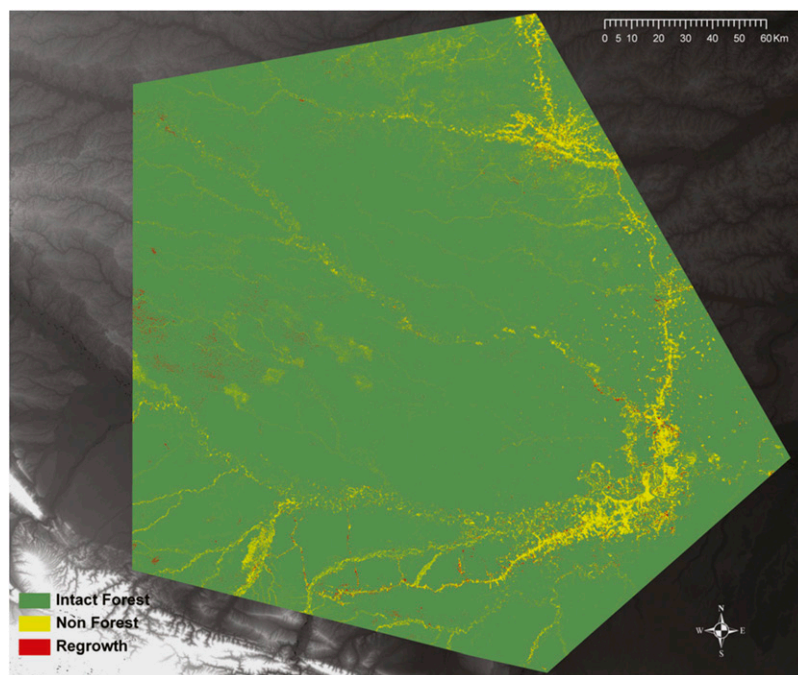
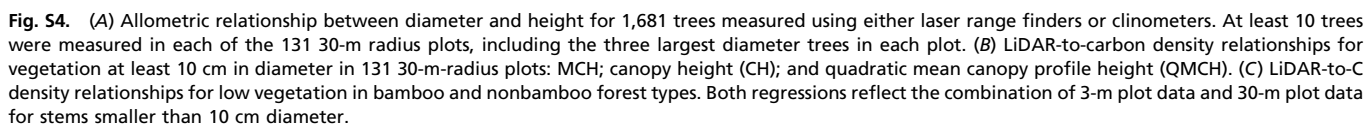


Fig. 53. CLASlite results showing forest cover (green), nonforest cover (yellow), and secondary forest regrowth (red) at 30 m spatial resolution, integrated over the period 1999 to 2009.



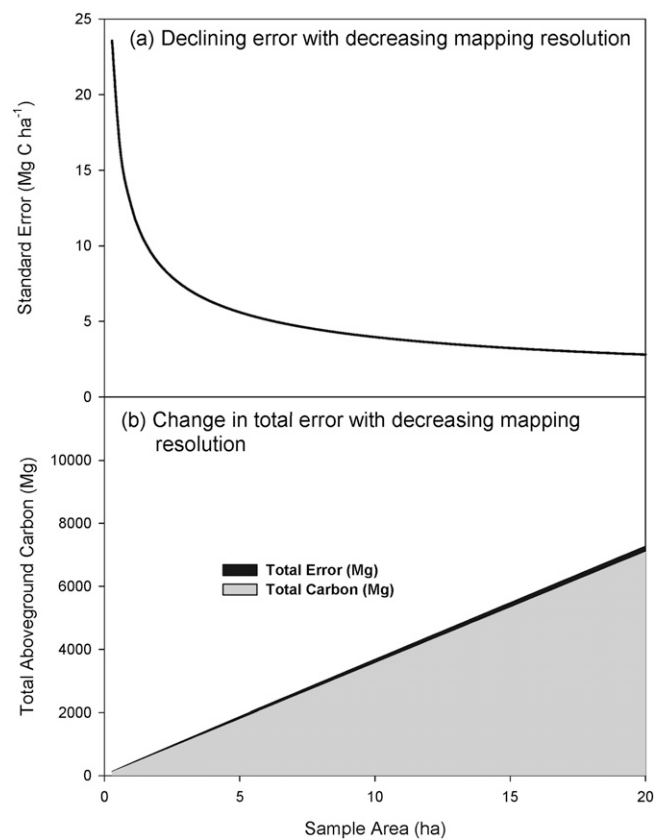


Fig. S7. Absolute (A) and relative (B) errors in LiDAR-based estimates of aboveground carbon densities decrease with decreasing mapping resolution as a result of an averaging effect described in [SI Materials and Methods](#).

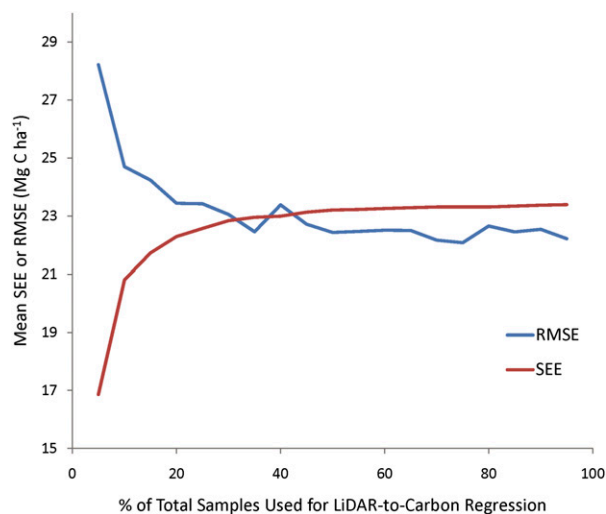


Fig. S8. Relationship between the number of field plots and the rmse and SEE of the LiDAR-to-carbon density regression.

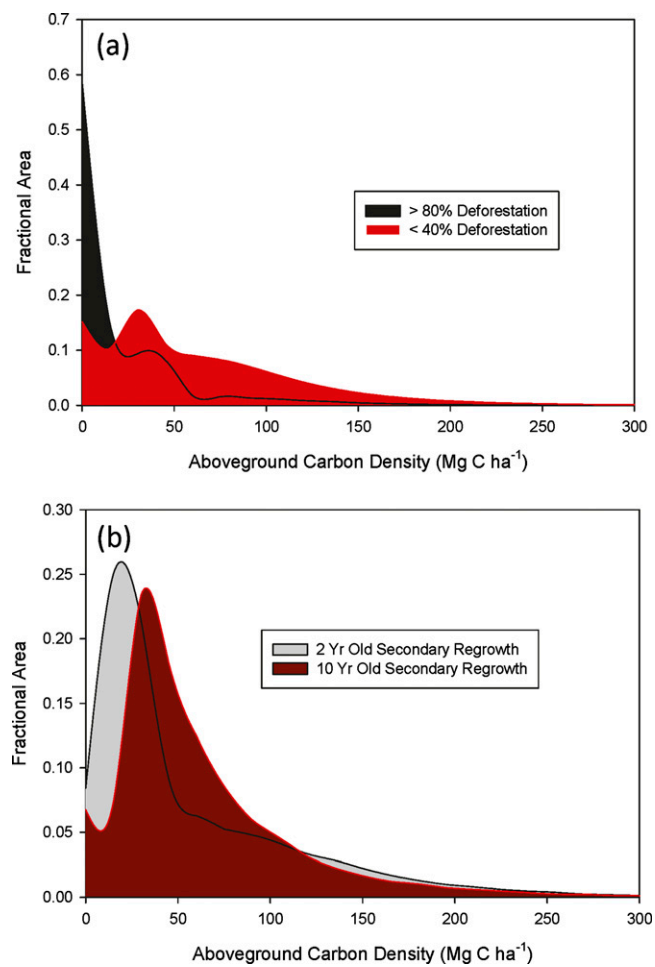


Fig. S10. Distribution of aboveground carbon for areas with (A) greater than 80% or less than 40% deforested canopy cover, and (B) secondary forest regrowth of 2 and 10 y following initial clearing.

Table S1. MINAM vegetation classes mapped in the study region and the airborne LiDAR sampling coverage of each class

Vegetation class	Total area, km ²	LiDAR area, km ²	Cover, %
Forest on high terraces with Brazil nut stands	10,212.5	643.6	6.3
Forest on low hills with bamboo	7,444.9	409.2	5.5
Forest on low hills	4,770.7	210.7	4.4
Swamp with trees	3,331.1	298.4	9.0
Forest on high terrace with bamboo	3,049.3	183.7	6.0
Human-affected areas	2,861.6	160.3	5.6
Forest on low flood terraces	1,786.8	183.7	10.3
Forest on high terraces with wetland areas	1,637.7	68.3	4.2
Forest on low flood terrace with bamboo	1,040.9	35.1	3.4
Forest on low hills with bamboo and rubber tree stands	1,032.9	39.0	3.8
Swamp forest with palm	786.4	84.4	10.7
Forest plains	774.3	198.4	25.6
Bamboo on low hills	772.7	24.5	3.2
Bamboo on high terraces	758.5	112.0	14.8
Forest on high hills	728.9	17.8	2.4
Forest on high hills with bamboo	671.8	36.1	5.4
River edges	631.7	82.7	13.1
Forest on medium terrace with bamboo	416.2	11.0	2.6
Forest on medium terraces	369.4	115.8	31.4
Forest on low hills with rubber tree stands	133.3	0.0	0.0
Forest on high terrace with bamboo and rubber stands	131.7	44.7	33.9
Forest on high terraces with rubber stands	123.0	27.1	22.0
Beaches and sand banks	56.3	11.3	20.0
Forest on medium terraces with swamped areas	44.1	0.0	0.0
Bamboo on medium terraces	41.2	0.6	1.5
Bamboo on low flood terraces	38.3	0.2	0.5
Bamboo on high hills	34.0	12.5	36.7
Swamp with shrubs	19.4	2.4	12.6

Table S2. Field validation results for forest cover, deforestation, degradation and secondary forest regrowth in the CLASlite imagery

	No	Yes (%)
Deforestation (2008–2009)		
Mapped	78	1 (1.2)
Not mapped	0	69 (0)
Degradation (2008–2009)		
Mapped	*	5 (6.4)
Not mapped	1	52 (1.9)
Regrowth (2000–2009)		
Mapped	*	2 (2.6)
Not mapped	1	34 (2.9)

*included in the deforestation group for no mapped/no field.

Table S3. Equations used to estimate aboveground biomass for 131 30-m radius field plots

Stem type	Equation
<i>Mauritia</i>	$(-0.00006 \cdot D^3 + 0.0037 \cdot D^2 - 0.0301 \cdot D + 0.0685) \cdot 1000$
<i>Guadua</i>	$5.4922 \cdot D - 19.516$
Lianas	$\exp(2.657 \cdot \ln(D) - 1.484)$
Other palms	$\pi \cdot (0.5 \cdot D)^2 \cdot \rho \cdot H / 10$
Dead Trees	$\pi \cdot (0.5 \cdot D)^2 \cdot (1.17 \cdot \rho - 0.21) \cdot H / 10 \cdot 0.5$
Height	$\exp(-0.0716 \cdot \ln(D)^2 + 0.9887 \cdot \ln(D) + 0.5685) \cdot 1.0244$
Chave moist	$0.0509 \cdot \rho \cdot D^2 \cdot H$

Fit of the height equation is shown in Fig S4A. Palm and dead tree biomass was estimated using the formula for volume of a cylinder, corrected for wood density, and in the case of dead trees for trunk taper and decay typical of standing dead Amazonian trees.